Nanoscale Advances

ROYAL SOCIETY OF CHEMISTRY

PAPER

View Article Online
View Journal | View Issue

Cite this: *Nanoscale Adv.*, 2023, **5**, 830

Direct fabrication of NbS_2 nanoflakes on carbon fibers by atomic layer deposition for ultrasensitive cardiac troponin I detection†

Yazhou Huang, *[a] Yunfei Zhang,[a] Junyan Lv,[a] Yinfeng Shao,[a] Dongfang Yang[b] and Yuan Cong[c]

Received 21st November 2022
Accepted 8th January 2023

DOI: 10.1039/d2na00827k

rsc.li/nanoscale-advances

The sensitive detection of cardiac troponin I (cTnI) is of great significance for the early diagnosis of acute myocardial infarction (AMI). Herein, in order to fabricate an electrochemical biosensor for ultrasensitive cTnI detection, atomic layer deposition (ALD) was employed to directly deposit NbS_2 nanoflakes (NFs) on carbon fiber paper (CFP). Due to the self-limiting reaction of ALD, NbS_2NFs were deposited uniformly and accurately on the surface of carbon fibers by controlling the number of ALD cycles, which ensured ultrasensitive detection. Precise regulation of the nanoscale morphology and electrochemical performance of NbS_2 nanoflakes *via* ALD cycles was observed in depth. Owing to the high surface area and conductivity, an anodic/cathodic current of ~3.01 mA of NbS_2NFs/CFP can be obtained. Subsequently, an electrochemical biosensor based on the excellent performance of NbS_2NFs/CFP was fabricated. The ultrasensitive detection of cTnI in a linear range of 1 fM to 0.1 nM with a detection limit of 0.32 fM was achieved.

1. Introduction

Acute myocardial infarction (AMI) with high mortality and morbidity is an extremely time-sensitive disease.[1–3] Cardiac troponin I (cTnI) has been proved to be a typical biomarker of AMI owing to its superior sensitivity and specificity for myocardial damage.[4] Therefore, the sensitive detection of cTnI is of great significance in the early diagnosis of AMI. Among many cTnI detection methods such as enzyme-linked immunosorbent assay (ELISA),[5,6] field-effect transistor-based biosensors,[7] fluorescence,[8] electrochemiluminescence (ECL),[9] radioimmunoassay (RIA)[10] and surface plasmon resonance (SPR) biosensors,[11] electrochemical (EC) detection is one of the most promising choices owing to the high sensitivity and low background noise.[12–17] As it should be, the high sensitivity of electrochemical detection highly depends on the surface material on the working electrode and its manufacturing method.

Two-dimensional (2D) transition metal dichalcogenide (TMDC) materials[18] have promising prospects in detecting biological molecules including miRNA,[19–22] protein[23] and others,[24–27] because of their excellent stability, biological affinity, and large surface area. However, there are obvious problems for traditional 2D TMDCs such as MoS_2,[28] WS_2 (ref. 29) and ReS_2.[30] Firstly, the detection response current of the electrode is insufficient owing to their poor conductivity from the semiconductor structures. In order to improve the response current, they are often mixed with other high conductivity materials, such as graphene,[31] MXenes,[21] *etc.*,[32] which leads to a decrease in the detection accuracy and stability. In addition, due to the 2D structure, conventional modification methods that physically adsorb materials on the electrode surface by van der Waals force, such as drop coating,[33,34] chemical vapor deposition (CVD)[35,36] and hydrothermal,[37,38] easily lead to the agglomeration of materials on the electrode surface rather than uniform distribution. More seriously, the agglomerations induce additional impedance and make the material easy to fall off from the electrode surface during the detection process, which destroy the detection accuracy and stability of the electrode. Therefore, it is necessary to find a new material and manufacturing method to promote 2D TMDCs in detecting biomolecules.

Hence, NbS_2, a new type of 2D TMDC, is paid attention to. It not only has the advantages of traditional 2D TMDCs, including stability, biological affinity and a large surface area, but also has the high conductivity of metal owing to its zero band gap structure, which makes it an ideal material to build an electrochemical detection platform.[39,40] In addition, the development of atomic layer deposition (ALD) technology makes it

[a]*Industrial Center, Nanjing Institute of Technology, Nanjing 211167, People's Republic of China. E-mail: huangyazhou@njit.edu.cn*

[b]*School of Energy and Power Engineering, Nanjing Institute of Technology, Nanjing 211167, People's Republic of China*

[c]*School of Materials Science and Engineering, Nanjing Institute of Technology, Nanjing 211167, People's Republic of China*

† Electronic supplementary information (ESI) available. See DOI: https://doi.org/10.1039/d2na00827k

possible to manufacture 2D material sensing electrodes.[41,42] Thanks to self-limiting chemical reactions, ALD can accurately control the deposition process and avoid the agglomeration of materials on the surface of the electrode.[43–46] Therefore, it is timely and meaningful that employing ALD to manufacture a NbS_2 sensing electrode for ultrasensitive cTnI detection.

In this work, ALD was employed to directly and precisely deposit NbS_2 nanoflakes (NFs) on carbon fiber paper (CFP) to fabricate an electrochemical biosensor for ultrasensitive cTnI detection. Precise regulation of the nanoscale morphology and electrochemical performance of NbS_2NFs *via* ALD cycles was observed. Then, the structure, mechanism and sensitivity of the biosensor were observed by various means.

2. Experimental

2.1. Materials

Carbon fiber paper (CFP, TGP-H-60) was purchased from Toray. Potassium chloride (KCl, 99.5%) and potassium hexacyanoferrate-II trihydrate ($K_4[Fe(CN)_6]\cdot 3H_2O$, 99.5%) were purchased from Sinopharm Chemical Reagent Co., Ltd (Shanghai, China). Niobium chloride ($NbCl_5$, 99.8%), hydrogen tetrachloroaurate trihydrate ($HAuCl_4\cdot 3H_2O$, 99.9%) and potassium hexacyanoferrate-III ($K_3[Fe(CN)_6]$, 99.5%) were purchased from Aladdin (Shanghai, China). Phosphate buffer solution (PBS, pH 7.4) and 6-mercaptohexanol (MCH) were purchased from Sigma Aldrich (Shanghai, China). Nitrogen (N_2, 99.999%) and hydrogen sulfide (H_2S, 99.5%) were purchased from Nanjing Special Gas Co. Ltd Cardiac troponin I (cTnI), horseradish peroxidase (HRP), myoglobin (MB), nucleolin (NCL), and thiolated cTnI aptamer (AcTnI): 5′-SH-(C)6-CGTGCAGTACGCCAACCTTTCTCATGCGCGCTGCCCCTCTTA-3′ were purchased from Sangon Biotech Co., Ltd (Shanghai, China).

2.2. Fabrication of the electrochemical biosensor based on ALD-constructed NbS_2NFs/CFP

As shown in Fig. 1, NbS_2 NFs were firstly deposited on the surface of carbon fiber paper (CFP, 0.25 cm^2) by ALD. $NbCl_5$ and H_2S were selected as Nb and S sources for ALD respectively. An ALD cycle consists of four steps: feeding $NbCl_5$ (0.5 s), purging $NbCl_5$ (10 s), feeding H_2S (0.5 s), and purging H_2S (10 s). The corresponding two self-limiting reactions can be given as follows.

$$(A)\ \ Nb-SH^* + NbCl_5 \rightarrow Nb-S-NbCl_4^* + HCl$$

$$(B)\ NbCl^* + H_2S \rightarrow Nb\text{–}SH^* + HCl + S$$

where * denotes the surface species. Due to the self-limiting chemical reactions, the depositing process of NbS_2NFs can be accurately controlled by the number of ALD cycles. During the ALD process, the reaction chamber and $NbCl_5$ were kept at 430 and 130 °C respectively. In addition, the pressure of the reaction chamber was controlled at 10 hPa, and 100 sccm of N_2 was used as the carrying and purging gas.

In order to assemble the cTnI aptamer (AcTnI) probe, Au nanoparticles (AuNPs) were electrodeposited on NbS_2NFs/CFP in 20 mL electrolyte solution composed of 0.02 g $HAuCl_4\cdot 3H_2O$ and 0.15 g KCl at a constant potential of −0.2 V for 200 s. Then, 15 μL AcTnI probe (1 μM) solution was dripped and assembled on the surface of NbS_2NFs/CFP with AuNPs (named AcTnI/Au/NbS_2NFs/CFP). The unbound AuNPs were filled by 6-mercaptohexanol (MCH) to avoid nonspecific adsorption, through adding 15 μL MCH solution (1 μM) on AcTnI/Au/NbS_2NFs/CFP (named MCH/AcTnI/Au/NbS_2NFs/CFP). Thus, the

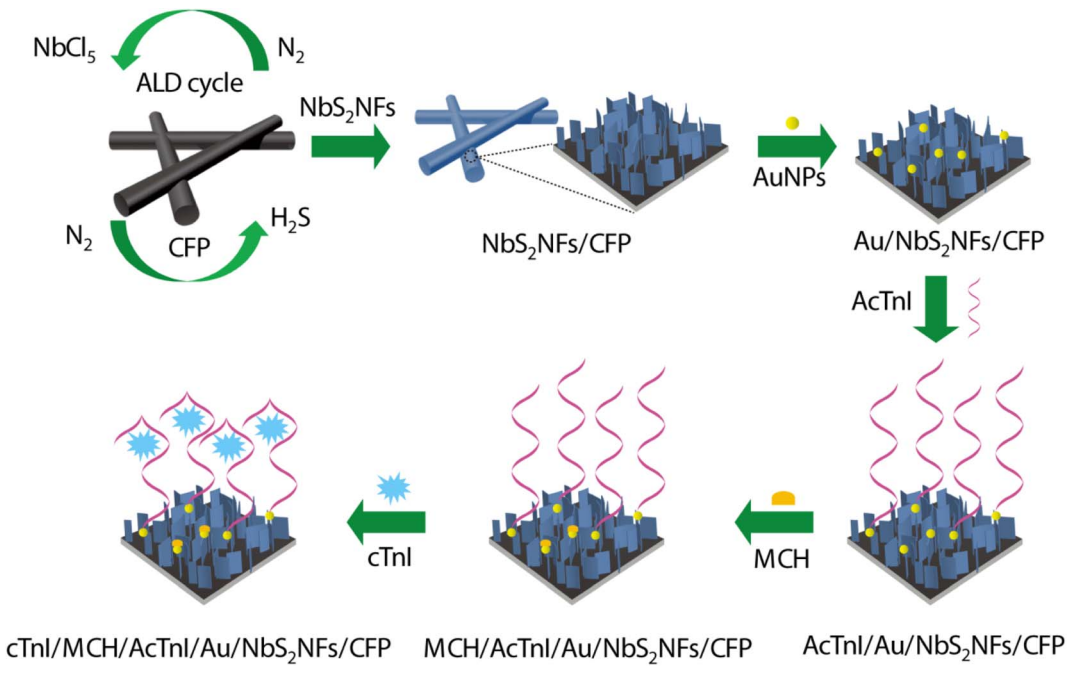

Fig. 1 Schematic showing the fabrication of the electrochemical biosensor and its detection of cTnI.

sensing platform was built. Different concentrations of cTnI can be captured by the AcTnI probe owing to the specific binding (named cTnI/MCH/AcTnI/Au/NbS_2NFs/CFP), and then detected through the decrease of electrochemical current owing to the steric hindrance effect.

2.3. Techniques

The morphology, chemical elements and crystal structures of as-constructed NbS_2NFs/CFP were observed by various means, including atomic force microscopy (AFM, Dimension Icon, Bruker), scanning electron microscopy (SEM, S-4800, Hitachi), high resolution transmission electron microscopy (HRTEM, Talos F200X G2, FEI), energy dispersive spectroscopy (EDS, S-4800, Hitachi), X-ray photoelectron spectroscopy (XPS, EscaLab-250Xi, Thermo Fisher), Raman spectroscopy (Reflex, Renishaw) and X-ray diffraction (XRD, D8 Advance, Bruker). Before TEM characterization, the samples were ground into powder and transferred on a copper grid. HRTEM was performed using an accelerating voltage of 200 kV. Raman spectroscopy was carried out by using excitation light of a 532 nm laser with 0.8 mW power and 1 μm spot. XRD was carried out with Cu Kα radiation ($\lambda = 1.54$ Å) at 40 mA and 45 kV. The XPS source is Al Kα ($h\nu = 1486.6$ eV) with a power of 22.8 W.

All the electrochemical tests were carried out by using a three-electrode electrochemical cell (CHI660E, CH Instruments), which employed a saturated calomel electrode (SCE) and a Pt wire as reference and counter electrodes, in an electrolyte solution composed of 5 mM $[Fe(CN)_6]^{3-/4-}$, 0.1 M KCl and 0.1 M PBS. The electrochemical properties of NbS_2NFs/CFP were observed by cyclic voltammetry (CV), electrochemical impedance spectroscopy (EIS) and chronocoulometry (CC), respectively. CV was performed in a range of −0.2 and 0.6 V at a scan rate of 50 mV s^{-1}. EIS was performed from 0.1 to 100 kHz at the open circuit voltage. Chronocoulometry was performed in an electrolyte solution composed of 0.1 mM $[Fe(CN)_6]^{3-}$ and 1 M KCl with an initial potential of 0 V and a final potential of 0.4 V. Finally, the detection performance of the sensor for cTnI was evaluated by using the peak current of differential pulse voltammetry (DPV) in a range of −0.2 and 0.6 V.

3. Results and discussion

3.1. Deposition of NbS_2 nanoflakes by ALD

In order to evaluate ALD, NbS_2 was firstly deposited on flat SiO_2. The deposition process of NbS_2 can be accurately controlled by the ALD cycle, because of the self-limiting chemical reactions. NbS_2 films obtained by 10, 30 and 50 ALD cycles on SiO_2 substrates were scanned by AFM. As shown in Fig. 2(a)–(c) and S1,† with the increase of ALD cycles from 10 to 50, NbS_2 showed the typical process of nucleation, growth, and film formation. Then, the changes of the thickness, particle diameter and coverage of NbS_2 with the number of ALD cycles were observed

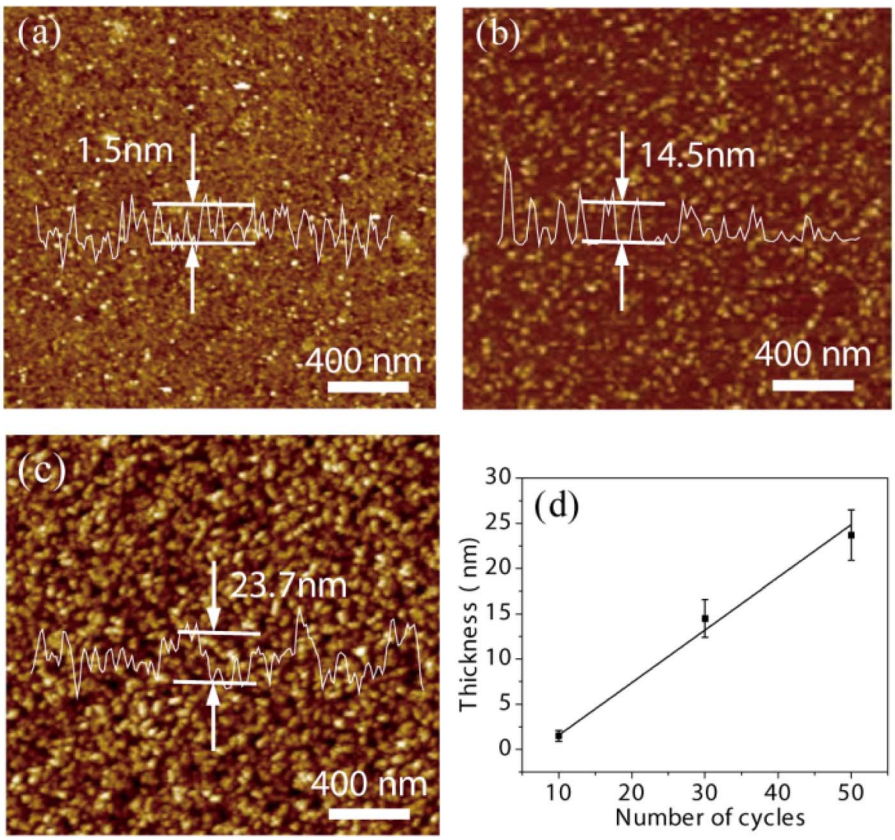

Fig. 2 AFM images of NbS_2 films obtained by 10 (a), 30 (b), and 50 (c) ALD cycles. (d) Thickness of the NbS_2 film against the number of ALD cycles.

in detail. When the number of ALD cycles increases from 10 to 30, the thickness, particle diameter and coverage increase from ~1.5 nm, ~3.3 nm and 18% to ~14.5 nm, ~23 nm and 48% respectively. After adding another 20 cycles, the thickness, particle diameter and coverage increase to ~23.7 nm, 30 nm and 83%. Growth-per-cycle (GPC) was usually employed to evaluate ALD. As shown in Fig. 2(d), the GPC of 0.58 nm is close to the single layer thickness (~0.6 nm) of natural NbS_2,[44] indicating the excellent performance of ALD.

Then NbS_2 was deposited on carbon fiber paper (CFP) to construct the sensing electrode. The SEM images of bare CFP and NbS_2NFs/CFP obtained by 10, 30, 50, 70 and 100 ALD cycles are shown in Fig. 3(a)–(f), which exhibit the precise growth process of NbS_2 nanoflakes under the control of the ALD cycle. According to Fig. 3(b), NbS_2 firstly nucleates uniformly on the CFP surface by 10 ALD cycles. It was further grown into NbS_2 nanoparticles after another 20 cycles, and its density also increased significantly at the same time (as shown in Fig. 3(c)). Then, when the number of ALD cycles reached 50 (Fig. 3(d)), NbS_2 nanoflakes of ~300 nm appeared on the basis of NbS_2 nanoparticles. This is an important moment meaning that NbS_2 nanoflakes have been successfully built on the CFP surface by ALD. However, it is obvious that the CFP substrate is not completely covered by the NbS_2 nanoflakes. As shown in Fig. 3(e), the NbS_2 nanoflakes increased to ~500 nm after 70 ALD cycles, and they almost completely and uniformly covered the CFP substrate. Undesirably, the agglomeration of NbS_2 nanoflakes appeared on the surface of CFP when the ALD cycles increased to 100 (as shown in Fig. 3(f)), which is not recommendable. Therefore, NbS_2 nanoflakes on CFP obtained by 70 ALD cycles were preliminarily employed as the sensing electrode.

The NbS_2 nanoflake structure may significantly increase the surface area of CFP and bind more AcTnI probes, thus improving the sensitivity in the electrochemical detection process. In addition, compared with the traditional 2D TMDCs such MoS_2, WS_2, ReS_2, *etc.*, NbS_2NFs will hardly induce additional resistance and reduce the response current of electrochemical detection, owing to its high conductivity.[47] Therefore, the excellent properties of NbS_2NFs/CFP including stability, biological affinity, a large surface area and high conductivity make it an ideal electrochemical sensing electrode. SEM results show that NbS_2 nanoflakes can be accurately constructed by ALD by controlling the number of cycles, thus avoiding the agglomeration of materials on the electrode surface and providing a guarantee for the accuracy and stability of the subsequent electrochemical biosensor.

In addition, the chemical elements of as-deposited NbS_2 nanoflakes by 70 ALD cycles were observed by EDS. As shown in Fig. 3(g), the S/Nb ratio is 1.56 indicating that the NbS_2

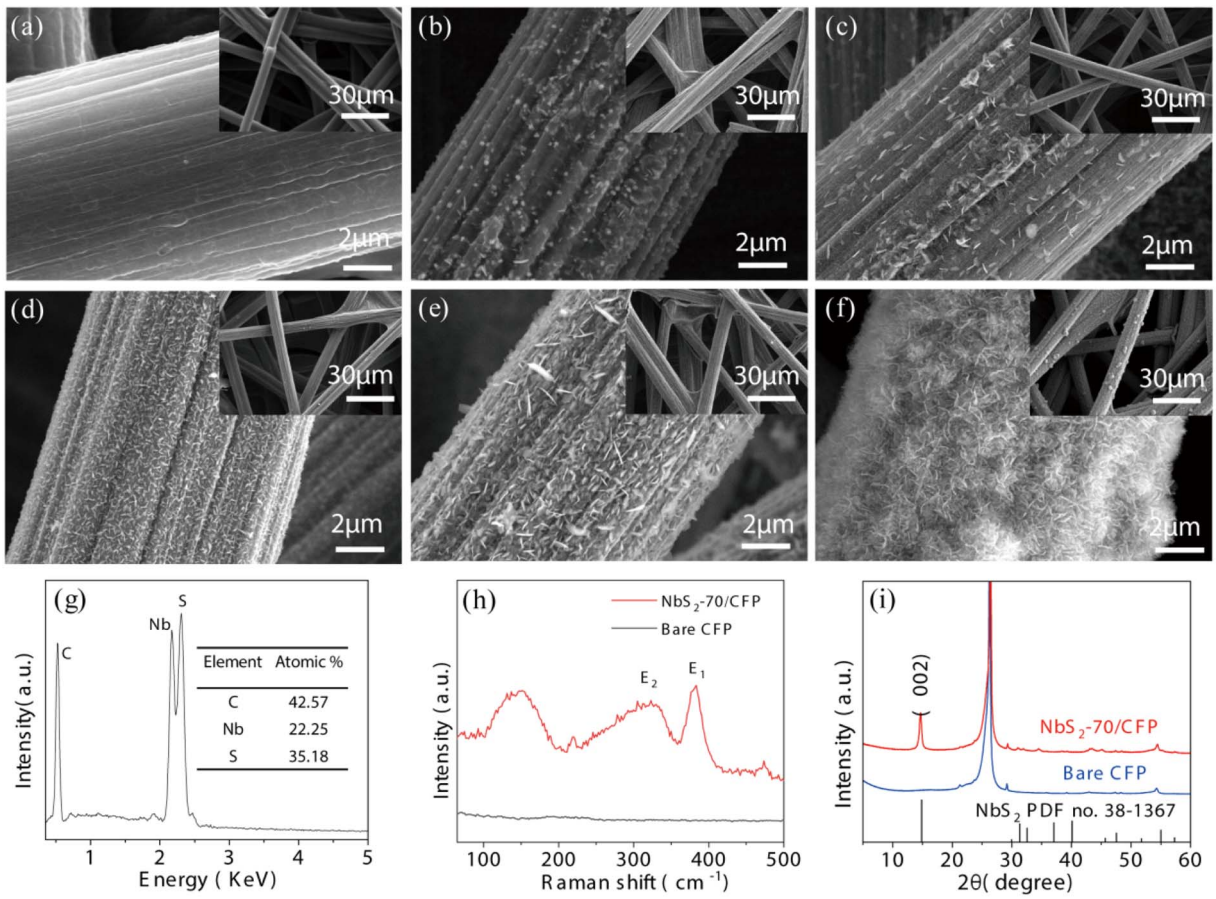

Fig. 3 SEM images of bare CFP (a) and NbS_2NFs/CFP obtained by 10 (b), 30 (c), 50 (d), 70 (e), and 100 (f) ALD cycles. ESD (g), Raman (h) and XRD (i) spectra of 70-NbS_2NFs/CFP.

nanoflakes are sulfur deficient. This can be attributed to the low temperature (450 °C) and the high efficiency (21 s per cycle) of the ALD process.[42] Raman (Fig. 3(h)) and XRD (Fig. 3(i)) of NbS_2NFs/CFP and bare CFP were also carried out at room temperature. As shown in Fig. 3(h), the NbS_2 peak at 321 cm^{-1} belongs to E_2 mode, and the peak at 381 is from its E_1 mode. According to Fig. 3(i), the (002) peak at 14.6° in the XRD spectrum confirms the 2H phase structure of NbS_2.[47]

The structures of the as-deposited NbS_2 nanoflakes by 70 ALD cycles were further observed by TEM. Fig. 4(a) shows the NbS_2 nanoflakes with a thickness of ~300 nm on the CFP. The elemental mapping under HAADF confirms the compositions of Nb and S of NbS_2 (Fig. 4(b)). According the HRTEM images in Fig. 4(c) and (d), a layer structure with a spacing of 0.6 nm can be clearly observed. In addition, the chemical elements were also observed by XPS. According to Fig. 4(e) and (f), the peaks of Nb $3d_{3/2}$, Nb $3d_{5/2}$, S $2p_{1/2}$ and S $2p_{3/2}$ are clearly shown at 210.68, 207.78, 165.08 and 163.88 eV respectively, which correspond to Nb^{4+} and S^{2-} of NbS_2.[47] Hence, the XPS results indicate that NbS_2 nanoflakes have been successfully constructed on the CFP.

3.2. Electrochemical performance of the NbS_2NFs/CFP electrode obtained by ALD

In order to find the most suitable one to fabricate the cTnI sensor, the electrochemical performance of bare CFP and as-deposited NbS_2NFs/CFP by different ALD cycles was evaluated by a cyclic voltammetry (CV) test. According to the CV curves shown in Fig. 5(a), for bare CFP, it can be observed that anodic/

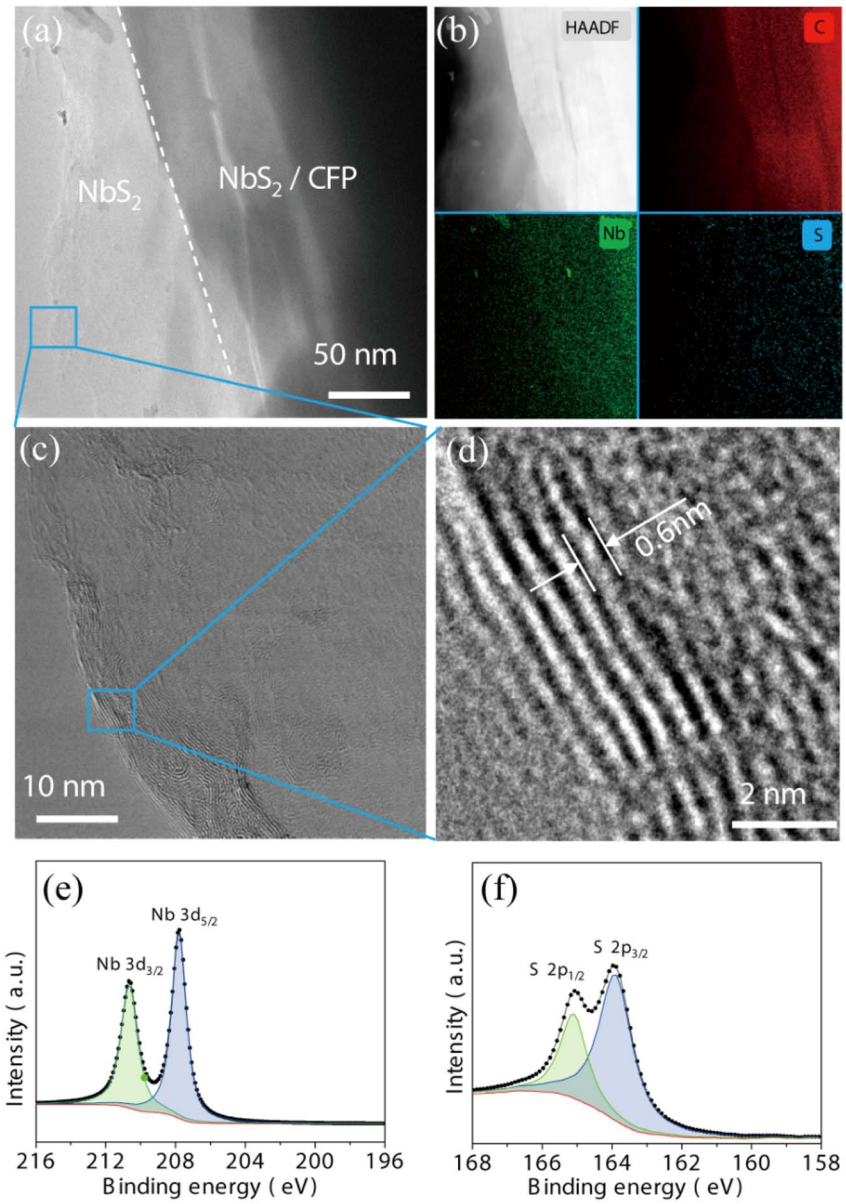

Fig. 4 (a) TEM image of NbS_2NFs/CFP. (b) High-angle annular dark-field (HAADF) images of the area in (a) and its elemental mapping images of C, Nb, and S, respectively. (c and d) HRTEM images of the local area in (a). XPS spectra of Nb 4f (e) and S 2p (f).

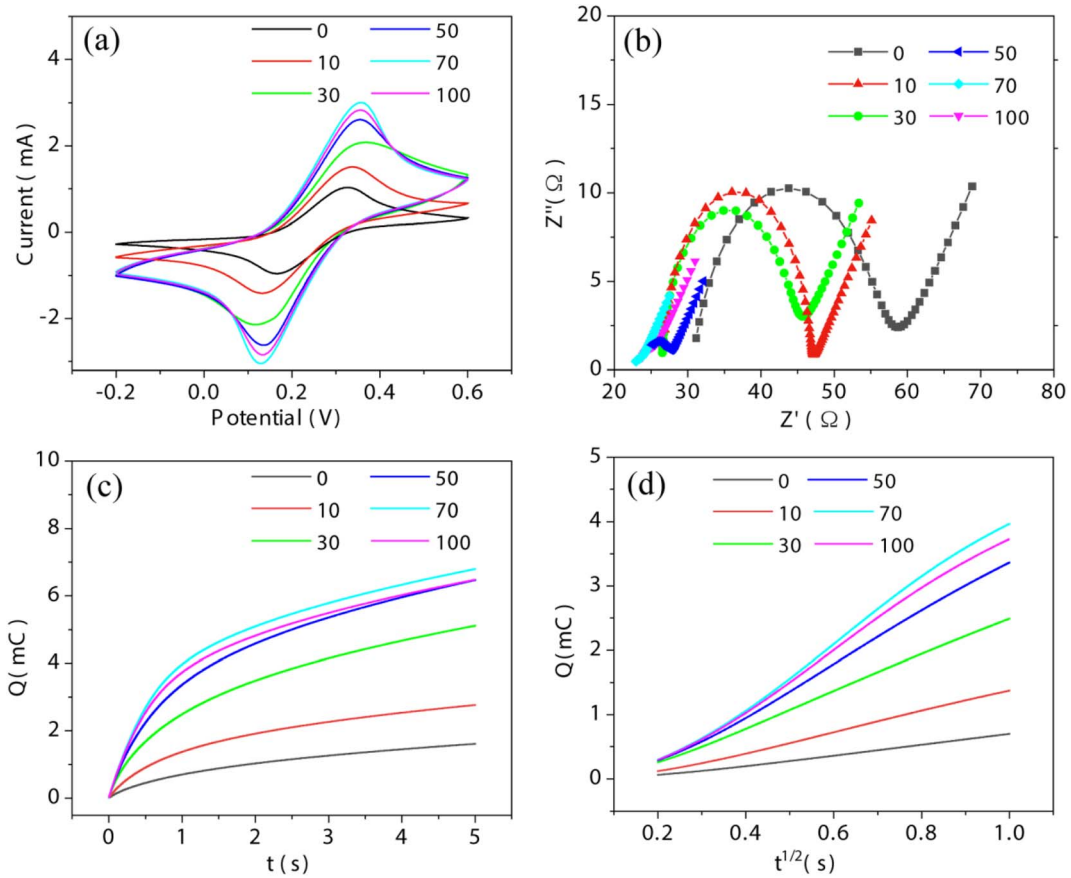

Fig. 5 (a) CV, (b) EIS, (c) Q–t, and (d) Q–$t^{1/2}$ curves of bare CFP and NbS_2NFs/CFP obtained by different ALD cycles. 0, 10, 30, 50, 70 and 100 are bare CFP, 10, 30, 50, 70 and 100 ALD cycles respectively.

cathodic current peaks with an intensity of ~1.03 mA appear at 0.32 and 0.16 V respectively. However, the currents were only ~0.2 mA while a conductive glass plane with the same size (0.25 cm^2) was selected as the electrode substrate.[41] The reason why CFP has such a high current intensity is its high specific surface area from a large number of voids scattered between the carbon fibers, which can improve the contact area between the electrode and the electrolyte. Therefore, the CFP electrode substrate ensures the high sensitivity of the subsequent sensors. However, by conventional methods, it is difficult to modify materials accurately and uniformly on the substrate surface with a high specific surface area like CFP. ALD can effectively solve this problem owing to the self-limiting reaction (shown in SEM images in Fig. 3). When NbS_2 nanoflakes were deposited on the surface of CFP by different ALD cycles, there was a significant increase in the currents. As the number of ALD cycles increases from 10 to 70, the intensity gradually enhances from ~1.51 to ~3.01 mA, because the NbS_2 nanoflakes with high conductivity further improve the contact between the electrode and the electrolyte. However, when the ALD cycle increases to 100, the current decreases by ~0.17 mA. This can be attributed to the agglomeration of NbS_2 nanoflakes on the CFP surface (shown in Fig. 3(f)), which reduces the contact between the electrode and the electrolyte, thus hindering the transfer of charge in the redox process.

The electrode dynamics of as-deposited NbS_2NFs/CFP were further observed by electrochemical impedance spectroscopy (EIS). EIS and the equivalent circuit are shown in Fig. 5(b) and S2.† The R_{CT}, meaning the resistance of charge transport at the interface between the electrode and the electrolyte, is indicated by the semicircle in the high-frequency region in EIS. For bare CFP, R_{CT} is 26.29 Ω. When 10 ALD cycles of NbS_2 nanoflakes were deposited on the surface of CFP, R_{CT} dropped significantly to 20.06 Ω. Then, as the number of ALD cycles increases, the R_{CT} keeps decreasing and reaches the minimum (0.82 Ω) at 70 cycles, but there is an increase at 100 cycles (1.66 Ω). Obviously, the trends of the redox current and the R_{CT} are opposite with the number of ALD cycles. In other words, the increase of the redox current is due to the reduction of the R_{CT} by depositing NbS_2 nanoflakes on CFP. The results of EIS indicate that the alteration of the current is mainly caused by the change of the interface resistance, and ALD can precisely modify the electrode by controlling the number of cycles.

In addition, the effective surface area (ESA) between the electrode and the electrolyte was evaluated by using Anson's equation:[48] $Q = 2nFAcD^{1/2}t^{1/2} + Q_{dl} + Q_{ads}$. The Q–t and Q–$t^{1/2}$ curves of bare CFP and NbS_2NFs/CFP from chronocoulometry tests are shown in Fig. 5(c) and (d). Then, the ESA was obtained by the linear fitting of the Q–$t^{1/2}$ curve. The ESA of bare CFP is 1.28 cm^2, which is much larger than its geometry size (0.25 cm^2), owing to the large number of voids between the carbon

fibers in the CFP. The ESA of NbS_2NFs/CFP obtained by 10, 30, 50, 70 and 100 ALD cycles is 3.08, 5.37, 7.51, 9.26 and 8.62 cm^2 respectively. Obviously, NbS_2 nanoflakes on the surface of CFP further increase the ESA, and the NbS_2 nanoflakes obtained by 70 cycles get the largest one. Hence, the improvement of the interface resistance R_{CT} of NbS_2NFs/CFP is mainly due to the increase of the ESA by depositing NbS_2 nanoflakes.

Moreover, as one of the traditional 2D TMDCs, the electrochemical performance of MoS_2 nanoflakes obtained by 70 ALD cycles had also been observed for a contrast (Fig. S3†). Due to the poor conductivity, the current (~1.06 mA) of MoS_2NFs/CFP is much smaller than that of NbS_2NFs/CFP (~3.01 mA). Therefore, the reason why NbS_2NFs/CFP has such an excellent electrochemical performance is the large surface area and the high conductivity coming from the CFP substrate and the 2D NbS_2 nanoflake structure, which ensure high sensitivity for the subsequent cTnI sensor. ALD-deposited NbS_2NFs/CFP by 70 cycles was chose as the electrode for the subsequent fabrication of the cTnI sensor.

3.3. Sensitivity and selectivity for cTnI sensing

As shown in Fig. 1, based on the ALD-deposited NbS_2NFs/CFP electrode, an electrochemical cTnI sensor was fabricated from modified AuNPs (Au/NbS_2NFs/CFP), an AcTnI probe (AcTnI/Au/TaS_2NFs/CFP) and MCH (MCH/AcTnI/Au/NbS_2NFs/CFP), respectively. Then, the sensor was used to detect cTnI (10^{-10} M, cTnI/MCH/AcTnI/Au/NbS_2NFs/CFP). The related DPV and EIS curves are shown in Fig. 6(a) and (b). The peak current of DPV and the interface resistance R_{CT} for NbS_2NFs/CFP, Au/NbS_2NFs/CFP, AcTnI/Au/NbS_2NFs/CFP, MCH/AcTnI/Au/NbS_2NFs/CFP and cTnI/MCH/AcTnI/Au/NbS_2NFs/CFP are 1.79, 1.86, 1.62, 1.45, and 1.06 mA, and 0.82, 0.62, 23.75, 32.35, and 70.97 Ω, respectively. The results of DPV and EIS were coincident with each other, indicating that the electrochemical sensor for cTnI detection has been successfully fabricated. When cTnI is fed to it, cTnI can be captured by the AcTnI probe on the surface of the sensor owing to specific binding, and then detected through the decrease of DPV current from the steric hindrance effect. Moreover, as shown in Fig. 6(c) and (d), when 10^{-10} M cTnI was added into the sensor, the time and temperature of hybridization between cTnI and the AcTnI probe were optimized based on the peak current of DPV. It can be observed that the optimal hybridization time and temperature are 120 min and 37 °C, which are set as the working parameters of the sensor.

The detection performance of the as-fabricated biosensor was further evaluated. cTnI with different concentrations from 10^{-10} to 10^{-15} M was detected by the sensor. According to Fig. 7(a), as the concentration of cTnI increases, the DPV current gradually decreases, due to the increase of the charge transport resistance from the steric hindrance caused by more cTnI. The peak current I against the logarithm concentration c of cTnI is

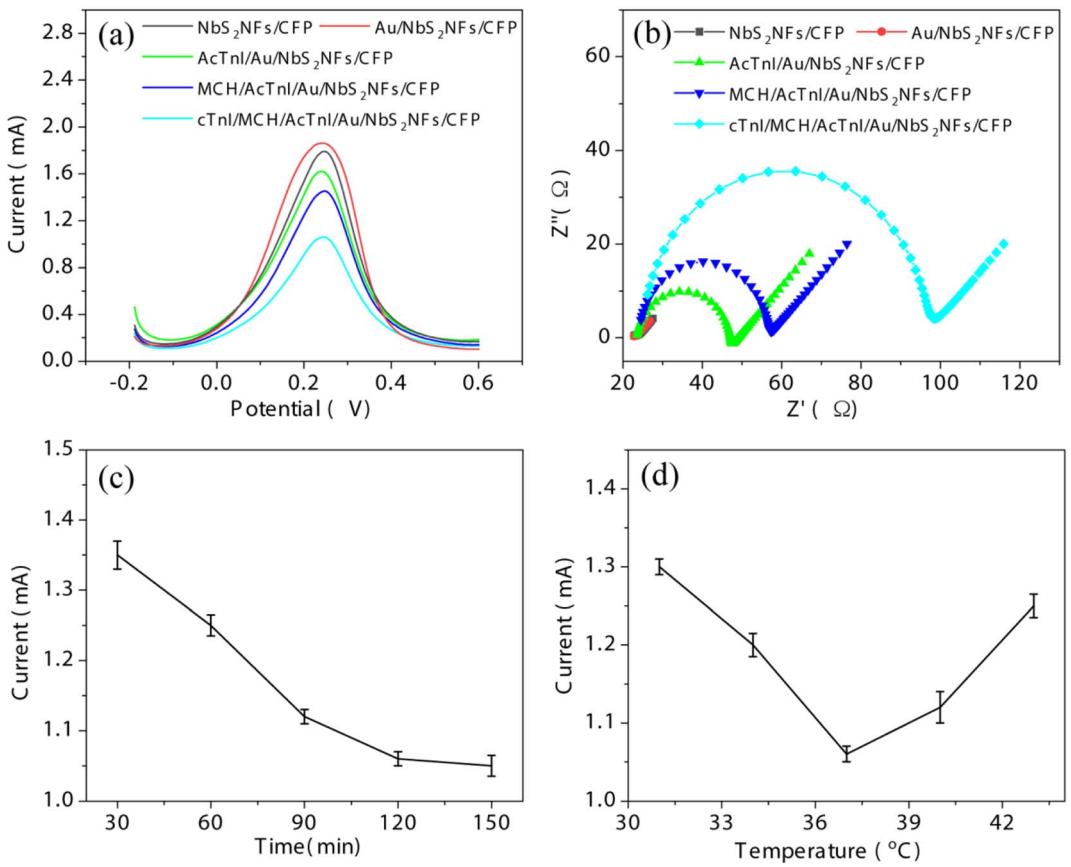

Fig. 6 (a) DPV and (b) EIS curves of different modifiers based on NbS_2NFs/CFP. The equivalent circuit is shown in Fig. S2.† Influence of the hybridization time (c) and temperature (d) on peak current ($n = 3$).

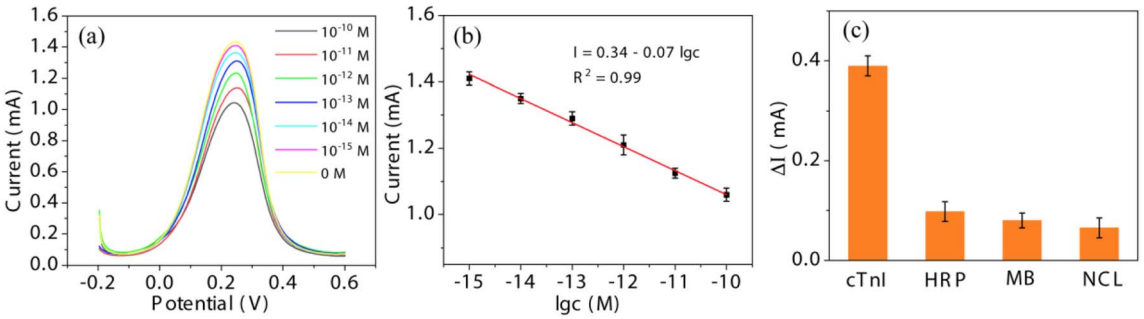

Fig. 7 (a) DPV response of the biosensor to various concentrations of cTnI (from 0 to 10^{-10} M). (b) The response current of (a) as a function of logarithm of concentration ($n = 3$). (c) Comparison of cTnI response current with other proteins (HRP, MB and NCL), indicating the excellent selectivity of the fabricated biosensor.

Table 1 Comparison of biosensing results for cTnI

Materials	Detection methods	Linear range (ng L^{-1})	LOD (ng L^{-1})	Ref.
N, Zn-G QDs	ECL	0.01–1000	0.005	13
BN QDs	DPV	10–5000	0.5	14
g-C_3N_4 QDs	Fluorescence	1–10 000	0.227	49
DPVBi	ECL	0.1–20 000	0.043	50
NbS_2NFs/CFP	DPV	0.022–2200 (1 fM–0.1 nM)	0.007 (0.32 fM)	This work

shown in Fig. 7(b). According to the linear relationship between I and c, $I = 0.34–0.07 \lg c$ can be obtained with a correlation coefficient $R^2 = 0.99$ and a limit of detection (LOD) of 0.32 fM (S/N = 3). The selectivity of the sensor was evaluated by using three other types of protein including horseradish peroxidase (HRP), myoglobin (MB) and nucleolin (NCL) at 10^{-10} M. According to Fig. 7(c), the DPV response ΔI of cTnI (0.39 mA) is much higher than that of HRP (0.098 mA), Mb (0.08 mA) and NCL (0.065 mA), indicating that the sensor has a high selectivity for cTnI. Moreover, compared with previous reports for cTnI detection (Table 1), the sensor based on ALD-constructed NbS_2NFs/CFP is potentially useful for the early diagnosis of AMI. Meanwhile, ALD is a simple and controllable method that can be employed in large-scale manufacturing of the electrochemical sensor.

3.4. Stability and serum sample analysis

Stability is important to the actual work of the sensor. In order to evaluate the stability, the as-fabricated sensor was kept at 4 °C for 0–8 days. As shown in Fig. S4,† after 8 days, the current response lost only 12.26%, indicating good stability.

Finally, in order to evaluate the possibility of application in real samples, the performance of the as-fabricated sensor was observed in serum. As shown in Table S1,† recoveries for cTnI with different concentrations (100 pM, 1 pM and 10 fM) are 101.61, 93.67 and 99.23 respectively, and the relative standard deviation (RSD) is less than 5%, indicating the effective detection of cTnI in real samples.

4. Conclusion

In summary, an electrochemical biosensor based on ALD-deposited NbS_2NFs/CFP for AMI-related cTnI detection has been successfully fabricated. Due to the self-limiting reactions, the nanoscale morphology and electrochemical performance of NbS_2 nanoflakes can be accurately and directly regulated by controlling the ALD cycles. Therefore, the agglomerations can be effectively avoided. An anodic/cathodic current of ~3.01 mA of NbS_2NFs/CFP deposited by 70 cycles can be obtained owing to its high surface area and conductivity. Then, the ultrasensitive detection of cTnI in a linear range of 1 fM to 0.1 nM with a detection limit of 0.32 fM was achieved at 37 °C with a hybridization time of 120 min. Hence, it is potentially useful for the early diagnosis of AMI and can be employed in large-scale manufacturing.

Author contributions

Y. H. conceptualization, writing-original draft, methodology, and writing-review & editing. Y. Z. formal analysis and methodology. J. L. and Y. S. methodology and data curation. D. Y. and Y. C. resources and conceptualization.

Conflicts of interest

There are no conflicts to declare.

Acknowledgements

This work was supported by the National Natural Science Foundation of China (51905259), the Natural Science Foundation of Jiangsu Province (BK20191017), the Qing Lan Project of Jiangsu Province, and the College Students' Practice and Innovation Training Program of Jiangsu Province (202211276020Z).

References

1 U. Friess and M. Stark, Cardiac Markers: A Clear Cause for Point-Of-Care Testing, *Anal. Bioanal. Chem.*, 2009, **393**(5), 1453–1462.

2 X. Liu, Y. Wang, P. Chen, A. McCadden, A. Palaniappan, J. Zhang and B. Liedberg, Peptide Functionalized Gold Nanoparticles With Optimized Particle Size and Concentration for Colorimetric Assay Development: Detection of Cardiac Troponin I, *ACS Sens.*, 2016, **1**(12), 1416–1422.

3 X. Han, S. Li, Z. Peng, A. M. Othman and R. Leblanc, Recent Development of Cardiac Troponin I Detection, *ACS Sens.*, 2016, **1**(2), 106–114.

4 M.-I. Mohammed and M. P. Y. Desmulliez, Lab-on-a-chip based immunosensor principles and technologies for the detection of cardiac biomarkers: a review, *Lab Chip*, 2011, **11**(4), 569–595.

5 E. Dempsey and D. Rathod, Disposable Printed Lateral Flow Electrochemical Immunosensors for Human Cardiac Troponin T, *IEEE Sens. J.*, 2018, **18**(5), 1828–1834.

6 I.-H. Cho, E.-H. Paek, Y.-K. Kim, J.-H. Kim and S.-H. Paek, Chemiluminometric enzyme-linked immunosorbent assays (ELISA)-on-a-chip biosensor based on cross-flow chromatography, *Anal. Chim. Acta*, 2009, **632**(2), 247–255.

7 K. Kim, C. Park, D. Kwon, D. Kim, M. Meyyappan, S. Jeon and J.-S. Lee, Silicon nanowire biosensors for detection of cardiac troponin I (cTnI) with high sensitivity, *Biosens. Bioelectron.*, 2016, **77**, 695–701.

8 P. Kar, A. Pandey, J. J. Greer and K. Shankar, Ultrahigh sensitivity assays for human cardiac troponin I using TiO_2 nanotube arrays, *Lab Chip*, 2012, **12**(4), 821–828.

9 C. A. Marquette, F. Bouteille, B. P. Corgier, A. Degiuli and L. J. Blum, Disposable screen-printed chemiluminescent biochips for the simultaneous determination of four point-of-care relevant proteins, *Anal. Bioanal. Chem.*, 2009, **393**(4), 1191–1198.

10 F. S. Apple, A. Falahati, P. R. Paulsen, E. A. Miller and S. W. Sharkey, Improved detection of minor ischemic myocardial injury with measurement of serum cardiac troponin I, *Clin. Chem.*, 1997, **43**(11), 2047–2051.

11 Y. Yanase, T. Hiragun, T. Yanase, T. Kawaguchi, K. Ishii and M. Hide, Application of SPR Imaging Sensor for Detection of Individual Living Cell Reactions and Clinical Diagnosis of Type I Allergy, *Allergol. Int.*, 2013, **62**(2), 163–169.

12 N. Singh, P. Rai, M. A. Ali, R. Kumar, A. Sharma, B. D. Malhotra and R. John, A hollow-nanosphere-based microfluidic biosensor for biomonitoring of cardiac troponin I, *J. Mater. Chem. B*, 2019, **7**(24), 3826–3839.

13 M. Liu, R. Jiang, M. Zheng, M. Li, Q. Yu, H. Zhu, H. Guo and H. Sun, A sensitive ratiometric biosensor for determination cardiac troponin I of myocardial infarction markers based on N, Zn-GQDs, *Talanta*, 2022, **249**, 123577.

14 M. L. Yola and N. Atar, Development of cardiac troponin-I biosensor based on boron nitride quantum dots including molecularly imprinted polymer, *Biosens. Bioelectron.*, 2019, **126**, 418–424.

15 D. Sun, Z. Luo, J. Lu, S. Zhang, T. Che, Z. Chen and L. Zhang, Electrochemical dual-aptamer-based biosensor for nonenzymatic detection of cardiac troponin I by nanohybrid electrocatalysts labeling combined with DNA nanotetrahedron structure, *Biosens. Bioelectron.*, 2019, **134**, 49–56.

16 I. Grabowska, N. Sharma, A. Vasilescu, M. Iancu, G. Badea, R. Boukherroub, S. Ogale and S. Szunerits, Electrochemical Aptamer-Based Biosensors for the Detection of Cardiac Biomarkers, *ACS Omega*, 2018, **3**(9), 12010–12018.

17 D. Sun, X. Lin, J. Lu, P. Wei, Z. Luo, X. Lu, Z. Chen and L. Zhang, DNA nanotetrahedron-assisted electrochemical aptasensor for cardiac troponin I detection based on the co-catalysis of hybrid nanozyme, natural enzyme and artificial DNAzyme, *Biosens. Bioelectron.*, 2019, **142**, 111578.

18 Q. H. Wang, K. Kalantar-Zadeh, A. Kis, J. N. Coleman and M. S. Strano, Electronics and optoelectronics of two-dimensional transition metal dichalcogenides, *Nat. Nanotechnol.*, 2012, **7**(11), 699–712.

19 S. Su, W. Cao, W. Liu, Z. Lu, D. Zhu, J. Chao, L. Weng, L. Wang, C. Fan and L. Wang, Dual-mode electrochemical analysis of microRNA-21 using gold nanoparticle-decorated MoS_2 nanosheet, *Biosens. Bioelectron.*, 2017, **94**, 552–559.

20 S. Su, Y. Wu, D. Zhu, J. Chao, X. Liu, Y. Wan, Y. Su, X. Zuo, C. Fan and L. Wang, On-Electrode Synthesis of Shape-Controlled Hierarchical Flower-Like Gold Nanostructures for Efficient Interfacial DNA Assembly and Sensitive Electrochemical Sensing of MicroRNA, *Small*, 2016, **12**(28), 3794–3801.

21 L. Liu, Y. Wei, S. Jiao, S. Zhu and X. Liu, A novel label-free strategy for the ultrasensitive miRNA-182 detection based on MoS_2/Ti_3C_2 nanohybrids, *Biosens. Bioelectron.*, 2019, **137**, 45–51.

22 L. Liu, M. Kong, Y. Xing, Z. Wu and Y. Chen, Atomic Layer Deposition-Made MoS_2–ReS_2 Nanotubes with Cylindrical Wall Heterojunctions for Ultrasensitive MiRNA-155 Detection, *ACS Appl. Mater. Interfaces*, 2022, **14**(8), 10081–10091.

23 S. Su, X. Han, Z. Lu, W. Liu, D. Zhu, J. Chao, C. Fan, L. Wang, S. Song, L. Weng, *et al.*, Facile Synthesis of a MoS_2–Prussian Blue Nanocube Nanohybrid-Based Electrochemical Sensing Platform for Hydrogen Peroxide and Carcinoembryonic Antigen Detection, *ACS Appl. Mater. Interfaces*, 2017, **9**(14), 12773–12781.

24 N. Rohaizad, C. C. Mayorga-Martinez, Z. Sofer and M. Pumera, 1T-Phase Transition Metal Dichalcogenides (MoS_2, $MoSe_2$, WS_2, and WSe_2) with Fast Heterogeneous Electron Transfer: Application on Second-Generation Enzyme-Based Biosensor, *ACS Appl. Mater. Interfaces*, 2017, **9**(46), 40697–40706.

25 T. Yang, M. Chen, F. Nan, L. Chen, X. Luo and K. Jiao, Enhanced electropolymerization of poly(xanthurenic acid)–MoS_2 film for specific electrocatalytic detection of guanine and adenine, *J. Mater. Chem. B*, 2015, **3**(24), 4884–4891.

26 N. Li, F. Zhang, W. Sun, L. Zhang and X. Su, Redox reaction-modulated fluorescence biosensor for ascorbic acid oxidase assay by using MoS_2 quantum dots as fluorescence probe, *Talanta*, 2021, **222**, 121522.

27 X. Lin, Y. Ni and S. Kokot, Electrochemical cholesterol sensor based on cholesterol oxidase and MoS_2-AuNPs modified glassy carbon electrode, *Sens. Actuators, B*, 2016, **233**, 100–106.

28 B. Radisavljevic, A. Radenovic, J. Brivio, V. Giacometti and A. Kis, Single-layer MoS_2 transistors, *Nat. Nanotechnol.*, 2011, **6**(3), 147–150.

29 R. J. Toh, C. C. Mayorga-Martinez, Z. Sofer and M. Pumera, 1T-Phase WS_2 Protein-Based Biosensor, *Adv. Funct. Mater.*, 2017, **27**(5), 1604923.

30 L. Liu, Y. Yao, K. Ma, C. Shangguan, S. Jiao, S. Zhu and X. Xu, Ultrasensitive photoelectrochemical detection of cancer-related miRNA-141 by carrier recombination inhibition in hierarchical Ti_3C_2@ReS_2, *Sens. Actuators, B*, 2021, **331**, 129470.

31 J. Zhou, Y. Zhao, J. Bao, D. Huo, H. Fa, X. Shen and C. Hou, One-step electrodeposition of Au-Pt bimetallic nanoparticles on MoS_2 nanoflowers for hydrogen peroxide enzyme-free electrochemical sensor, *Electrochim. Acta*, 2017, **250**, 152–158.

32 J. Yoon, T. Lee, B. Bapurao G, J. Jo, B.-K. Oh and J.-W. Choi, Electrochemical H_2O_2 biosensor composed of myoglobin on MoS_2 nanoparticle-graphene oxide hybrid structure, *Biosens. Bioelectron.*, 2017, **93**, 14–20.

33 J. Mei, Y.-T. Li, H. Zhang, M.-M. Xiao, Y. Ning, Z.-Y. Zhang and G.-J. Zhang, Molybdenum disulfide field-effect transistor biosensor for ultrasensitive detection of DNA by employing morpholino as probe, *Biosens. Bioelectron.*, 2018, **110**, 71–77.

34 B. Wang, X. Zhong, Y. Chai and R. Yuan, An ECL biosensor for sensitive detection of concanavalin A based on the ECL quenching of Ru complex by MoS_2 nanoflower, *Sens. Actuators, B*, 2017, **245**, 247–255.

35 J. Liu, X. Chen, Q. Wang, M. Xiao, D. Zhong, W. Sun, G. Zhang and Z. Zhang, Ultrasensitive Monolayer MoS_2 Field-Effect Transistor Based DNA Sensors for Screening of Down Syndrome, *Nano Lett.*, 2019, **19**(3), 1437–1444.

36 T. Pham, Y. Chen, J. Lopez, M. Yang, T.-T. Tran and A. Mulchandani, Effect of Al_2O_3 Passive Layer on Stability and Doping of MoS_2 Field-Effect Transistor (FET) Biosensors, *Biosensors*, 2021, **11**(12), 514.

37 S. Sri, D. Chauhan, G. B. V. S. Lakshmi, A. Thakar and P. R. Solanki, MoS_2 nanoflower based electrochemical biosensor for TNF alpha detection in cancer patients, *Electrochim. Acta*, 2022, **405**, 139736.

38 Y. J. Zhai, J. H. Li, X. Y. Chu, M. Z. Xu, F. J. Jin, X. Li, X. Fang, Z. P. Wei and X. H. Wang, MoS_2 microflowers based electrochemical sensing platform for non-enzymatic glucose detection, *J. Alloys Compd.*, 2016, **672**, 600–608.

39 J. Shi, X. Wang, S. Zhang, L. Xiao, Y. Huan, Y. Gong, Z. Zhang, Y. Li, X. Zhou, M. Hong, *et al.*, Two-dimensional metallic tantalum disulfide as a hydrogen evolution catalyst, *Nat. Commun.*, 2017, **8**(1), 958.

40 Y. Zhang, B. Zheng, C. Zhu, X. Zhang, C. Tan, H. Li, B. Chen, J. Yang, J. Chen, Y. Huang, *et al.*, Single-Layer Transition Metal Dichalcogenide Nanosheet-Based Nanosensors for Rapid, Sensitive, and Multiplexed Detection of DNA, *Adv. Mater.*, 2015, **27**(5), 935–939.

41 L. Liu, S. Zhu, Y. Wei, X. Liu, S. Jiao and J. Yang, Ultrasensitive detection of miRNA-155 based on controlled fabrication of AuNPs@MoS_2 nanostructures by atomic layer deposition, *Biosens. Bioelectron.*, 2019, **144**, 111660.

42 Y. Huang, L. Liu and X. Liu, Modulated electrochemical oxygen evolution catalyzed by MoS_2 nanoflakes from atomic layer deposition, *Nanotechnology*, 2019, **30**(9), 095402.

43 L. K. Tan, B. Liu, J. H. Teng, S. Guo, H. Y. Low and K. P. Loh, Atomic layer deposition of a MoS_2 film, *Nanoscale*, 2014, **6**(18), 10584–10588.

44 X. Peng, G. Wan, L. Wu, M. Zeng, S. Lin and G. Wang, Peroxidase-like activity of Au@TiO_2 yolk-shell nanostructure and its application for colorimetric detection of H_2O_2 and glucose, *Sens. Actuators, B*, 2018, (257), 166–177.

45 L. Yu, G. Wan, Y. Qin and G. Wang, Atomic layer deposition assisted fabrication of high-purity carbon nanocoil for electrochemical energy storage, *Electrochim. Acta*, 2018, (268), 283–294.

46 L. Wu, G. Wan, S. Shi, Z. He, X. Xu, Y. Tang, C. Hao and G. Wang, Atomic layer deposition-assisted growth of CuAl LDH on carbon fiber as a peroxidase mimic for colorimetric determination of H_2O_2 and glucose, *New J. Chem.*, 2019, **43**, 5826–5832.

47 Z. Li, W. Yang, Y. Losovyj, J. Chen, E. Xu, H. Liu, M. Werbianskyj, H. A. Fertig, X. Ye and S. Zhang, Large-size niobium disulfide nanoflakes down to bilayers grown by sulfurization, *Nano Res.*, 2018, **11**(11), 5978–5988.

48 F. C. Anson, Application of Potentiostatic Current Integration to the Study of the Adsorption of Cobalt(III)-Ethylenedinitrilo(tetraacetate) on Mercury Electrodes, *Anal. Chem.*, 1964, **36**(4), 932–934.

49 L. Miao, L. Jiao, Q. Tang, H. Li, L. Zhang and Q. Wei, A nanozyme-linked immunosorbent assay for dual-modal colorimetric and ratiometric fluorescent detection of cardiac troponin I, *Sens. Actuators, B*, 2019, **288**, 60–64.

50 M. Yan, S. Feng, L. Yu, Y. Xue, J. Huang and X. Yang, Label-free immunosensor for cardiac troponin I detection based on aggregation-induced electrochemiluminescence of a distyrylarylene derivative, *Biosens. Bioelectron.*, 2021, **192**, 113532.